Supporting Information

One-Dimensional Porous Li-Confinable Hosts for High-Rate and Stable Li-Metal Batteries

Dong Woo Kang,[†] Seong Soo Park,[‡] Hong Jun Choi,[†] Jun-Ho Park,[†] Ji Hoon Lee,[§] Sang-Min Lee,[#] Jeong-Hee Choi,[†,∥] Janghyuk Moon[,‡] and Byung Gon Kim*[,†,∥]*

[†] Next Generation Battery Research Center, Korea Electrotechnology Research Institute (KERI), 12 Jeongiui-gil, Seongsan-gu, Changwon-si, Gyeongsangnam-do 51543, Republic of Korea

[‡] School of Energy Systems Engineering, Chung-Ang University, 84 Heukseok-ro, Dongjakgu, Seoul 06974, Republic of Korea

[§] School of Materials Science and Engineering, Kyungpook National University, 80 Daehak-ro, Buk-gu, Daegu 41566, Republic of Korea

[#] Graduate Institute of Ferrous & Energy Materials Technology, Pohang University of Science and Technology (POSTECH), 77 Cheongam-Ro, Nam-gu, Pohang, Gyeongbuk 37673, Republic of Korea

[∥] Electro-functional Materials Engineering, University of Science and Technology (UST), 217 Gajeong-ro, Yuseong-gu, Daejeon 34113, Republic of Korea

* Email: (J.M.) jhmoon84@cau.ac.kr, (B.G.K.) byunggonkim@keri.re.kr

Method for Computational Simulation: Li deposition and growth behavior were simulated in a two-dimensional pseudo model (P2D) with Li asymmetric cell configurations implemented in COMSOL Multiphysics (ver. 5.5) FEM software.[S1] Three main governing equations were used to describe the mass movement of the charged species and the distribution of the electric and electrolyte potentials. According to Ohm's law, the current density vector i_s that flows through a cross-sectional area centered at a given location is proportional to the electric field and is calculated as follows:

$$i_s = -\sigma_s \nabla \emptyset_s \quad (1)$$

where σ_s is the material-dependent electrical conductivity and ϕ_s is the electric potential at a given location. The charge transfer behavior of the liquid electrolyte region can also be described by Ohm's law as:

$$i_l = (-\sigma_l \nabla \emptyset_l) + \frac{2\sigma_l RT}{F}\left(1 + \frac{\partial lnf}{\partial lnc_l}\right)(1 - t_+)\nabla lnc_l \quad (2)$$

where l indicates the liquid electrolyte region, σ_l is the ionic conductivity of the electrolyte, ϕ_l is the potential of the electrolyte, f is the molar activity coefficient, c_l is the concentration of the electrolyte salt, t_+ is the cation transference number, T is the temperature, R is the molar gas constant, and F is the Faraday constant.

The mass transport of Li ions in the liquid electrolyte region follows Fick's second law of diffusion:

$$\frac{\partial c_l}{\partial t} = \nabla \cdot (D_l \nabla c_l) - \frac{i_l t_+}{F} \quad (3)$$

where D_l is the diffusion coefficient of Li ion in the electrolyte.

In addition, the interfacial electrochemical kinetics were assumed to follow the generalized Butler–Volmer relationship. The charge transport behavior at the electrode–electrolyte interface can then be described as:

$$i = i_0 \left(\exp\left(\frac{(1-\alpha)F}{RT}\eta\right) - \exp\left(\frac{\alpha F}{RT}\eta\right)\right) \quad (4)$$

where i is the local current density at the interface between the electrode and electrolyte; α is the charge transfer coefficient; η is the overpotential, which is defined as the voltage difference between the electrode and electrolyte; and i_0 is the exchange current density, which is a different characteristic value between materials. The exchange current density was obtained from the Tafel plot. In this work, we calculated the exchange current densities of the PHCF, Au@HCF, and Au@PHCF as 0.0784, 0.1193, and 0.2363 mA cm^{-2}, respectively (Figure S9). The amount of deposited Li in the fiber can be obtained using the following equation:

$$\frac{\partial c_{LP}}{\partial t} = \frac{i_{LP}}{F} \quad (5)$$

where c_{LP} is the Li metal concentration in the fiber and i_{LP} is the local current density for the Li deposition in the fiber, which can be calculated using Eq. 4. The thickness of the deposited Li (δ_{film}) in the carbon fiber can be calculated by following equation:

$$\delta_{film} = \frac{c_{LP} \cdot M_{Li}}{\rho_{Li}} \quad (6)$$

where M_{Li} and ρ_{Li} are the molar mass and density of metallic Li, respectively. To describe the SEI layer, which is a product formed by a side reaction between the carbon fiber and the electrolyte, we designed the SEI layers inside and outside the carbon fiber to reflect the practical cell test environment.[S2] The electrolyte in the SEI layer region can be expressed by the following mass and charge conservation equations:

$$\frac{\partial c_{l,SEI}}{\partial t} = \nabla \cdot \left(D_{l,SEI} \nabla c_{l,SEI} \right) - \frac{i_{l,SEI} t_+}{F} \quad (7)$$

$$i_{l,SEI} = \left(-\sigma_{l,SEI} \nabla \emptyset_{l,SEI}\right) + \frac{2\sigma_{l,SEI} RT}{F}\left(1 + \frac{\partial lnf}{\partial lnc_{l,,SEI}}\right)(1 - t_+)\nabla lnc_{l,SEI} \quad (8)$$

where $c_{l,SEI}$ and $i_{l,SEI}$ are the electrolyte concentration and local current density in the SEI layer, respectively; $D_{l,SEI}$ and $\sigma_{l,SEI}$ are the diffusivity and conductivity of the electrolyte in the SEI layer,

respectively; and $\phi_{l,SEI}$ is the electrolyte potential of the SEI region. Owing to the morphology and characteristics of the SEI layer, the $D_{l,SEI}$ and $\sigma_{l,SEI}$ have poor values of 2.95×10^{-10} cm^2 s^{-1} and 1.1×10^{-6} S cm^{-1}, respectively, compared to those of the pure electrolyte (1.1×10^{-5} cm^2 s^{-1} and 1.1×10^{-2} S cm^{-1}, respectively).[S2] The values of the parameters used in this work are summarized in Table S2.

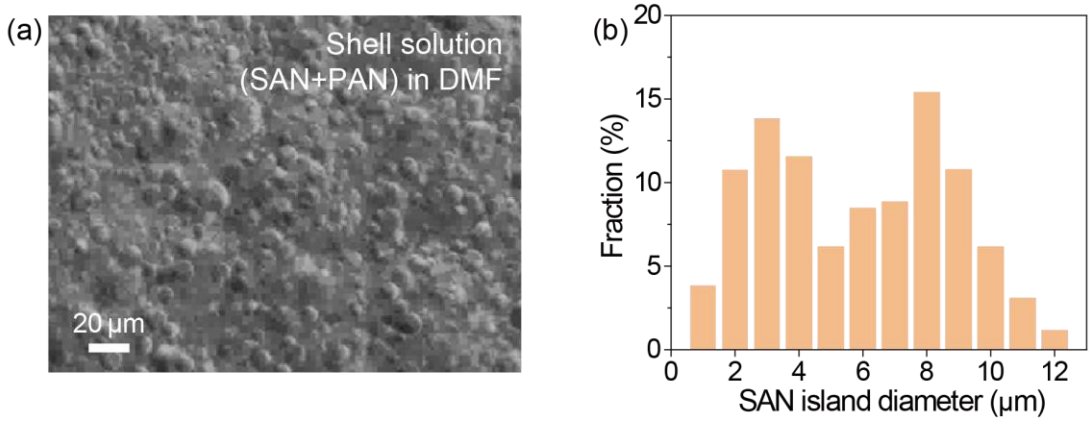

Figure S1. (a) Optical image of shell solution and (b) size distribution of SAN island in the solution.

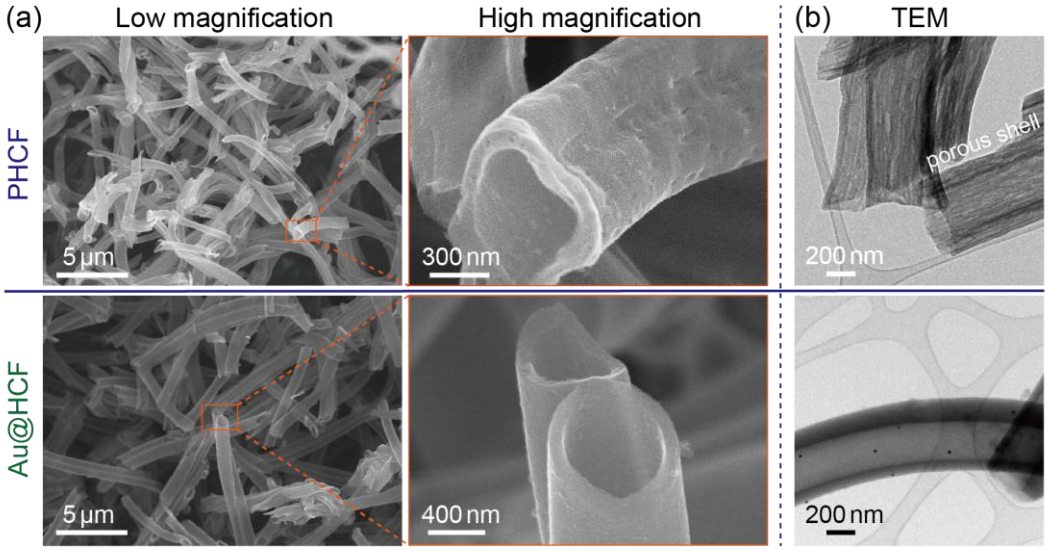

Figure S2. (a) SEM and (b) TEM images of pristine PHCF and Au@HCF samples.

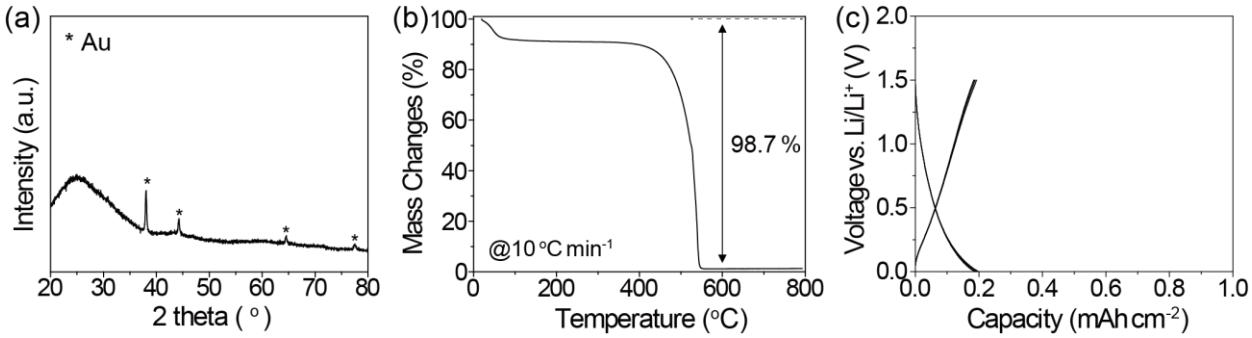

Figure S3. (a) XRD pattern of Au@PHCF powder showing the presence of Au. (b) TGA data of the Au@PHCF indicating that the weight percentage of Au in the sample is ~1.3 wt%. (c) Typical voltage profile of the PHCF electrode in the voltage range of 0.001–1.5 V at 1 mA cm^{-2}.

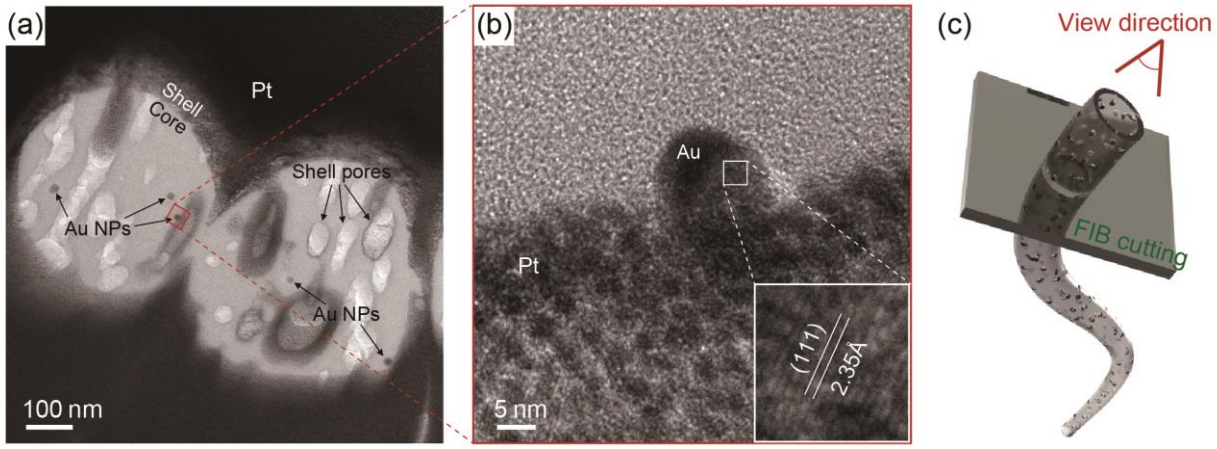

Figure S4. Cross-sectional (a) low- and (b) high-magnified TEM images of Au@PHCF showing the presence of Au NPs inside the core space of Au@PHCF. The inset in (b) is a high-resolution image marked by a red box in (a). For this TEM observation, (c) focused ion beam (FIB) and Pt coating were applied during sample preparation.

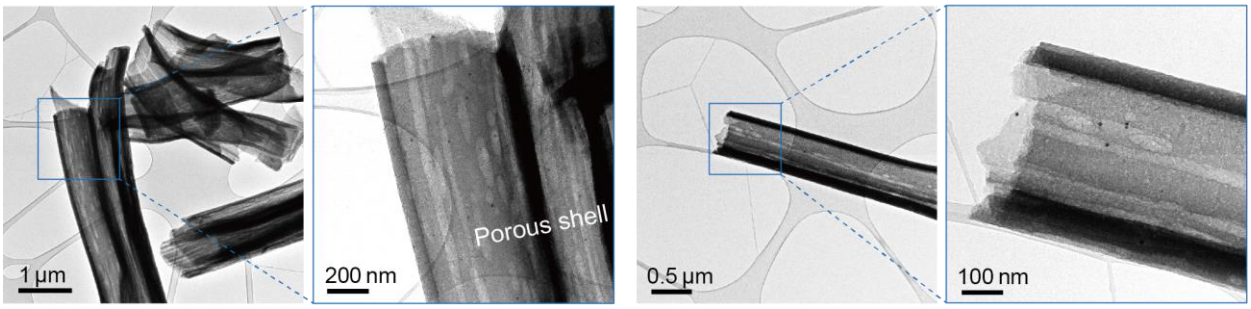

Figure S5. TEM images of pristine Au@PHCF at various viewpoints.

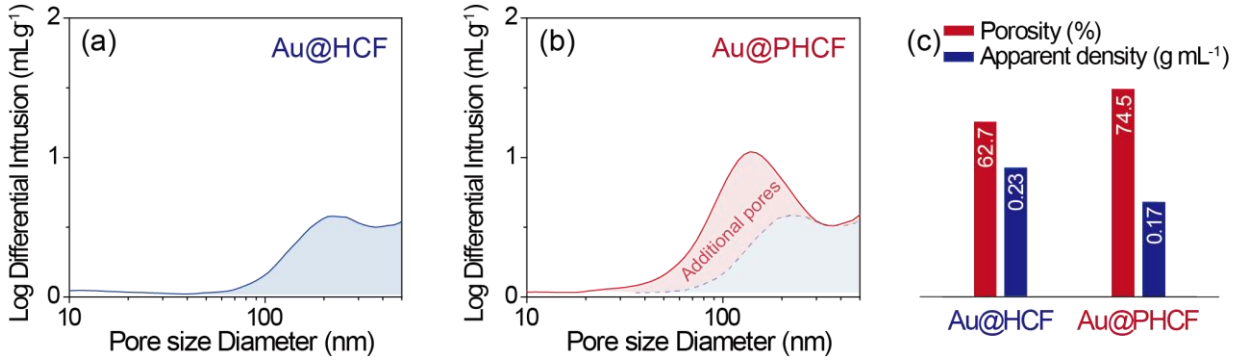

Figure S6. (a-b) Pore size distributions and (c) porosity and apparent densities of Au@HCF and Au@PHCF measured by mercury pore analysis.

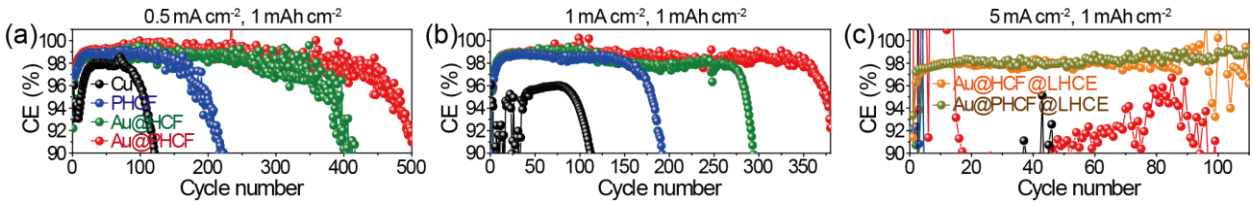

Figure S7. Enlarged CE plots shown in Figure 2a–c in the CE range of 90–101 %.

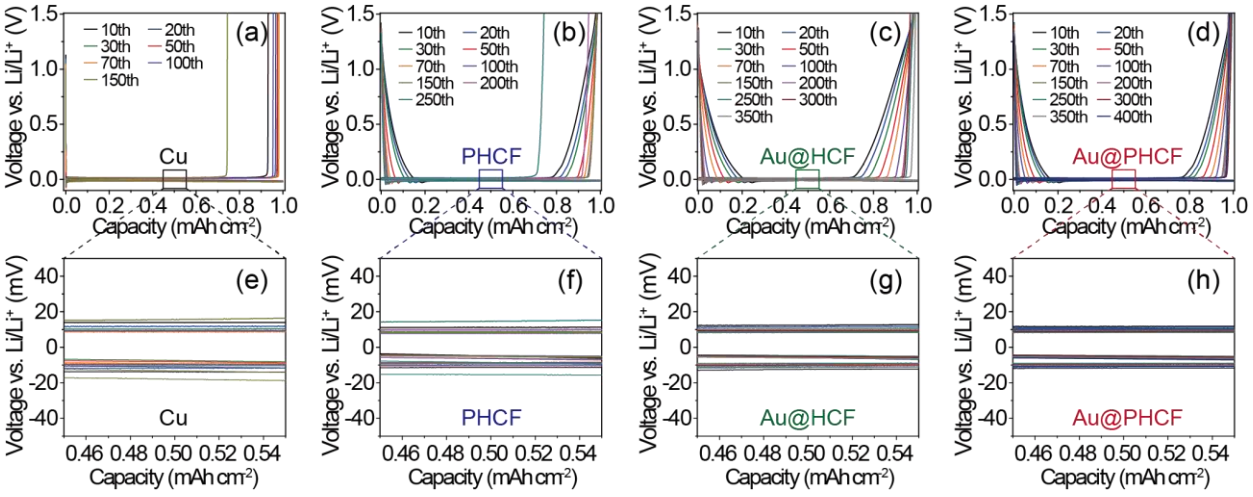

Figure S8. Voltage profiles of Cu, PHCF, Au@HCF, and Au@PHCF electrodes during CE tests shown in Figure 2a.

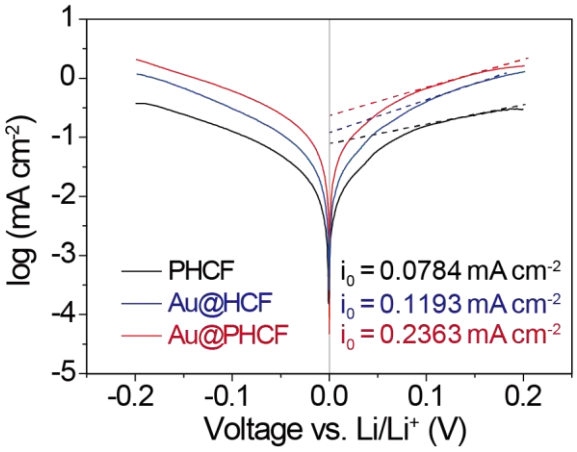

Figure S9. Tafel plots and derived exchange current densities of PHCF, Au@HCF, and Au@PHCF obtained from CV tests in Li/anode cells at a scan rate of 0.5 mV s^{-1}.

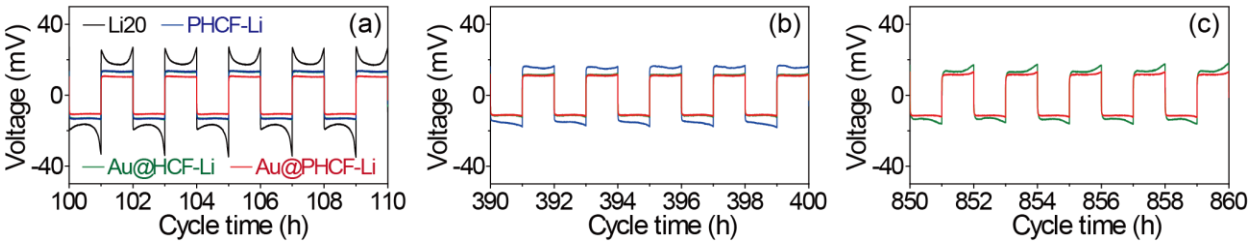

Figure S10. Detailed voltage profiles enlarged from the colored boxes shown in Figure 2e.

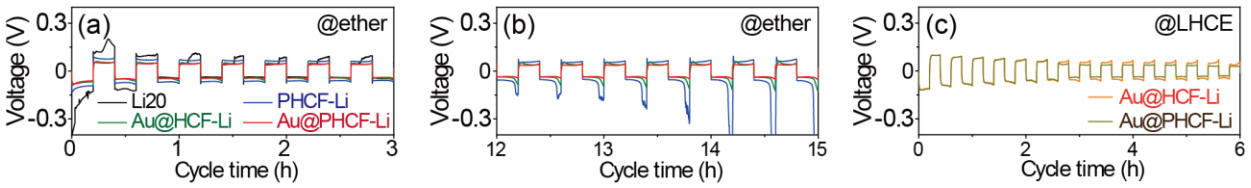

Figure S11. Detailed voltage profiles enlarged from the colored boxes in (a,b) Figure 2f and (c) 2g.

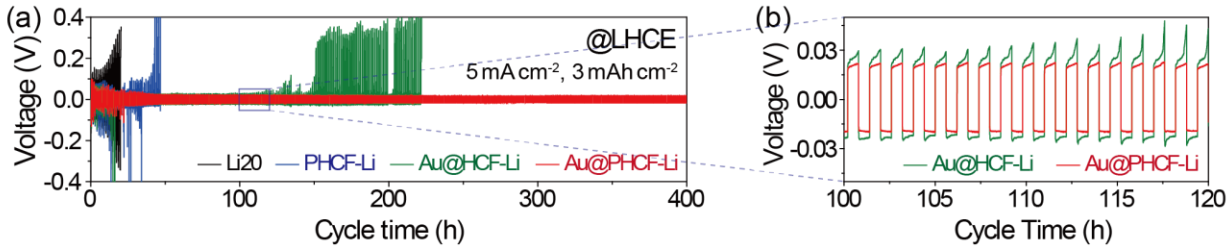

Figure S12. (a) Voltage profiles of symmetric cells containing Li20, PHCF-Li, Au@HCF-Li, and Au@PHCF-Li electrodes at 5 mA cm^{-2} with an operating capacity of 3 mAh cm^{-2}. (b) Detailed voltage profiles enlarged from the colored boxes shown in (a).

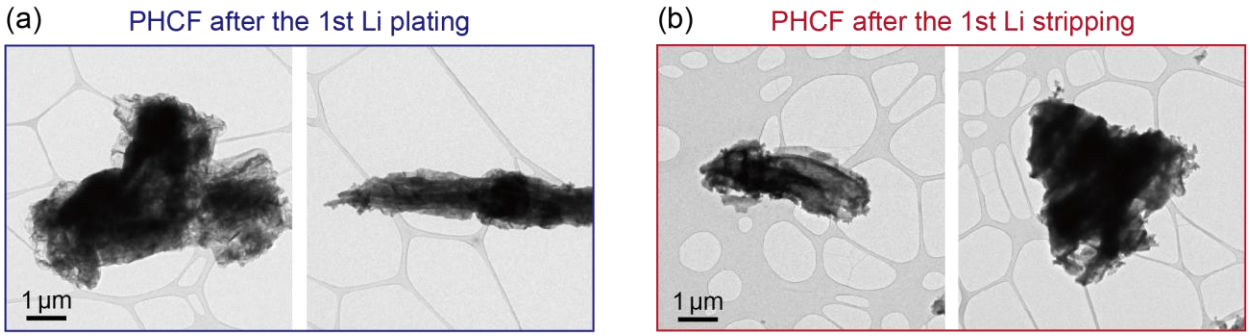

Figure S13. TEM images of PHCF after the 1st (a) Li plating and (b) stripping processes at 0.5 mA cm^{-2}.

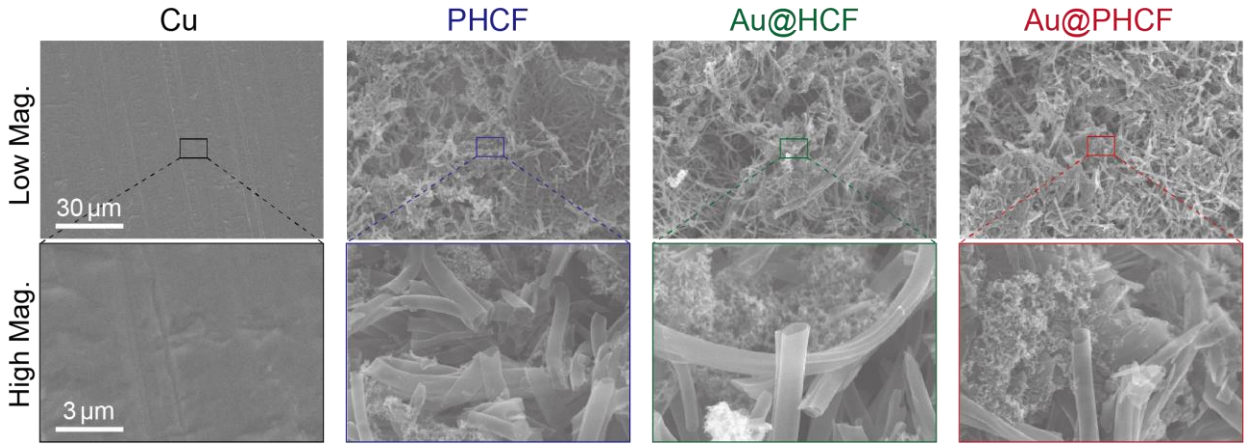

Figure S14. SEM images of pristine Cu, PHCF, Au@HCF, and Au@PHCF electrodes for this study.

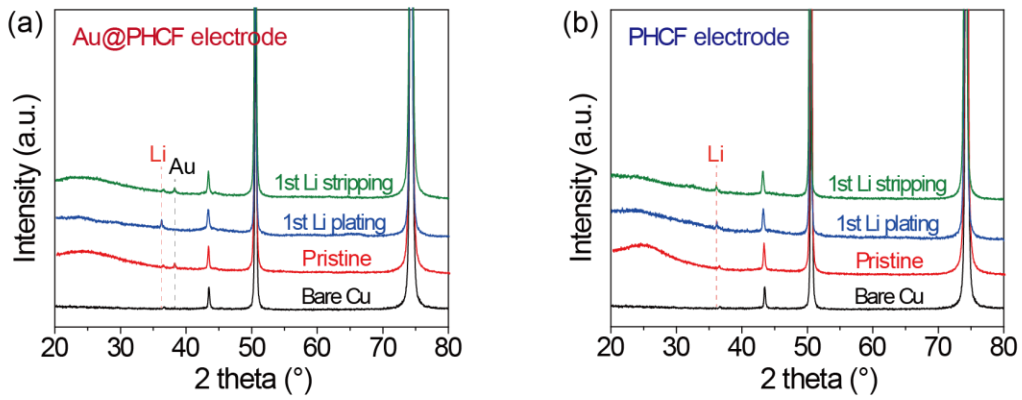

Figure S15. XRD spectra of (a) Au@PHCF and (b) PHCF electrodes at the pristine, 1st Li plated, and 1st Li stripped states.

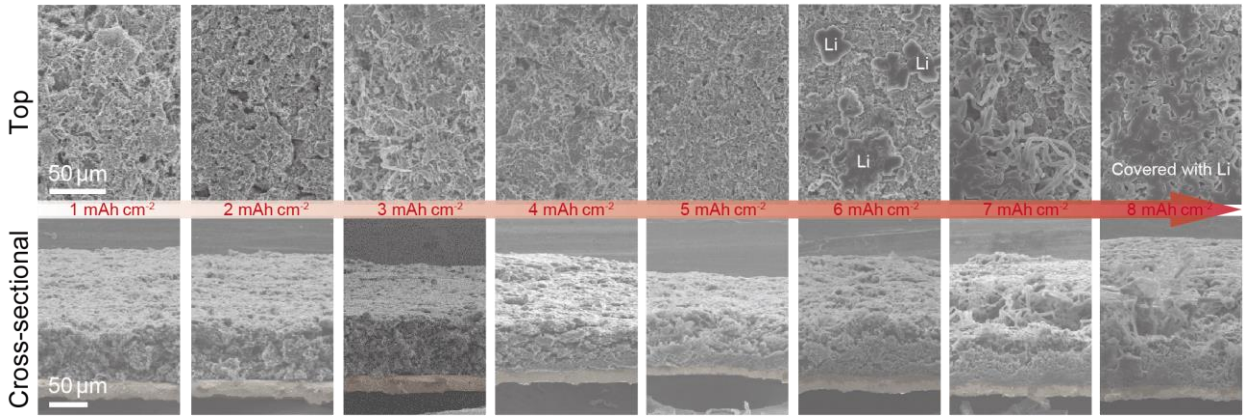

Figure S16. SEM images of the Au@PHCF electrode as the Li plating capacity increased at 1 mA cm^{-2}.

Note: Before the Li plating capacity exceeded the theoretical capacity of Au@PHCF, no noticeable Li top plating was observed because of the preferential Li deposition toward the core space of the host. However, when the Li plating capacity exceeded the theoretical capacity, the Li top plating on the Au@PHCF began to be observed. These results support the Li-confinable feature of the Au@PHCF.

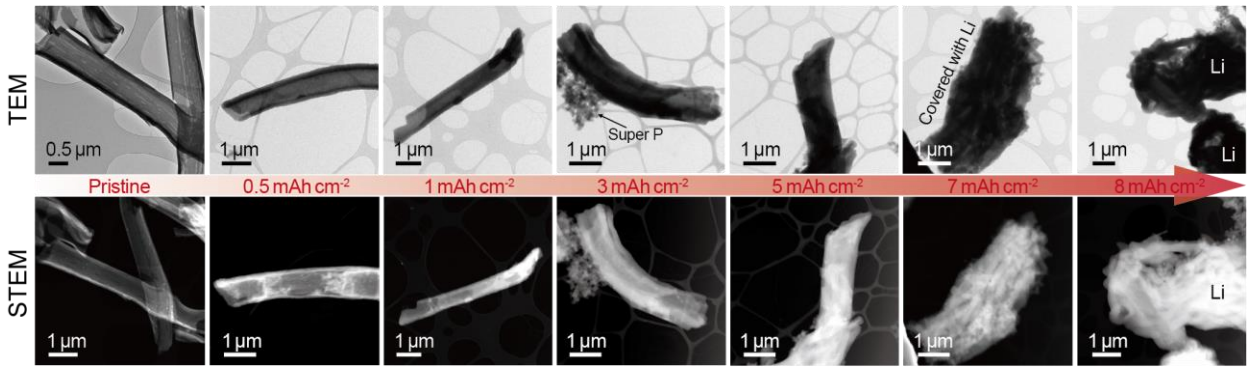

Figure S17. TEM (top row) and STEM (bottom row) images of Au@PHCF as the Li plating capacity increased from 0 to 8 mAh cm^{-2} at a current density of 1 mA cm^{-2}.

Note: Before the Li plating capacity reached the theoretical capacity of Au@PHCF, most of the Li was stored inside the Au@PHCF. However, when the Li plating capacity reached the theoretical capacity, Li deposition outside the Au@PHCF shell began to occur, which trend is similar to the SEM results shown in Figure S16.

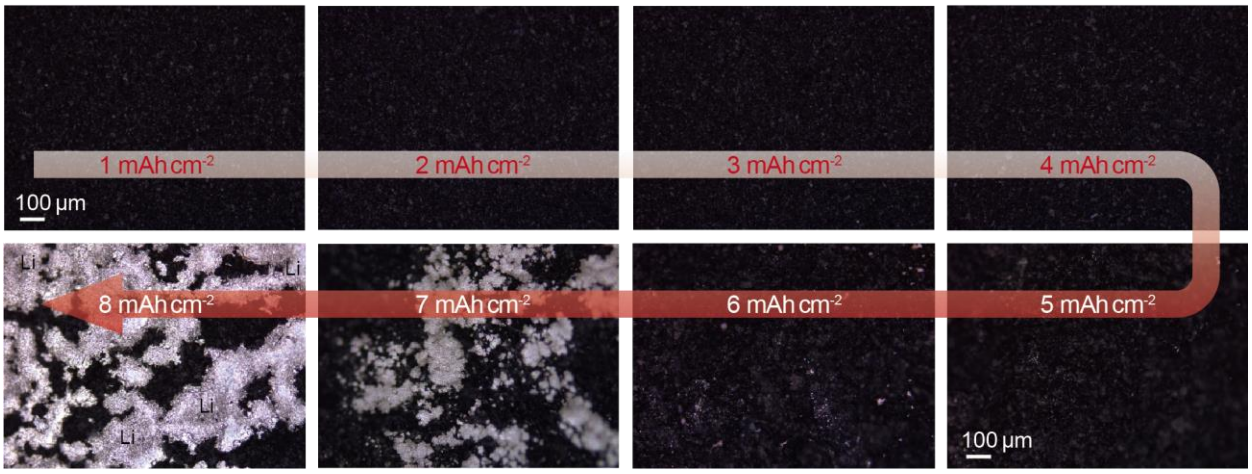

Figure S18. In situ top-view OM images at different Li plating capacities at 1 mA cm^{-2}.

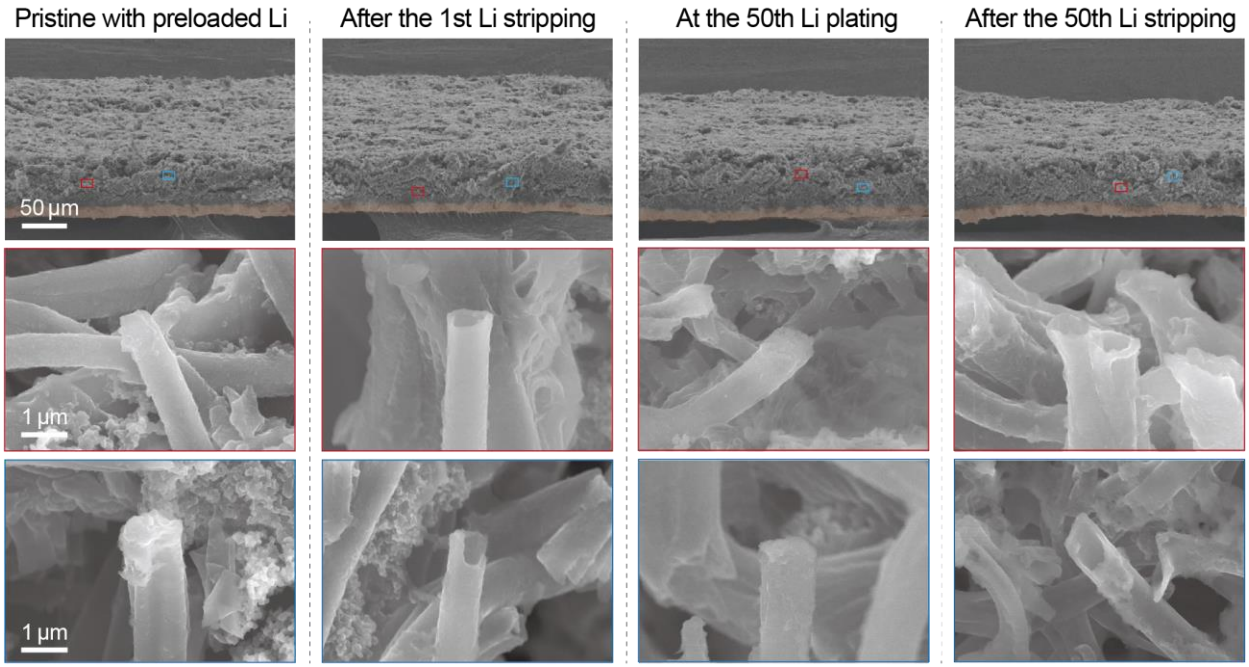

Figure S19. (Top row) Cross-sectional SEM images at the 1st and 50th cycles during symmetric cell cycling shown in Figure 2e. (Middle and bottom rows) Enlarged images of red and blue boxes shown in the low-magnification SEM images (top row).

Note: In the Li-preloaded Au@PHCF electrode used for the symmetric cell test, the core of Au@PHCF was filled with some matter identified as Li through XRD (Figure S15a). This Li disappeared after Li stripping and reappeared after Li plating process during 50 cycles. These results demonstrate the Li-confinable feature of Au@PHCF.

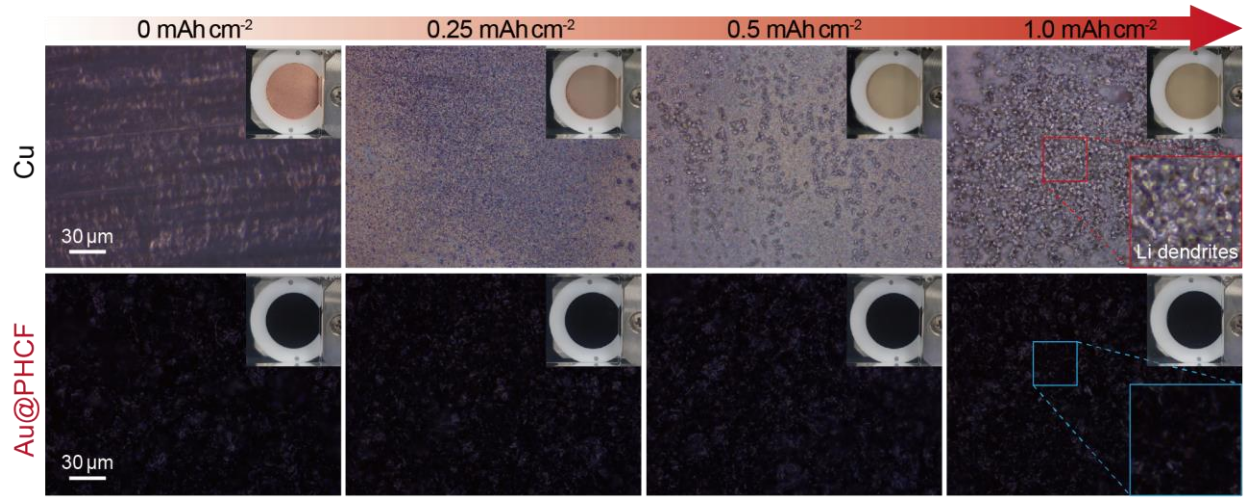

Figure S20. In situ OM images taken at various times during Li plating at 5 mA cm^{-2}. The insets are enlarged views of the colored boxes and digital photographs of the electrodes.

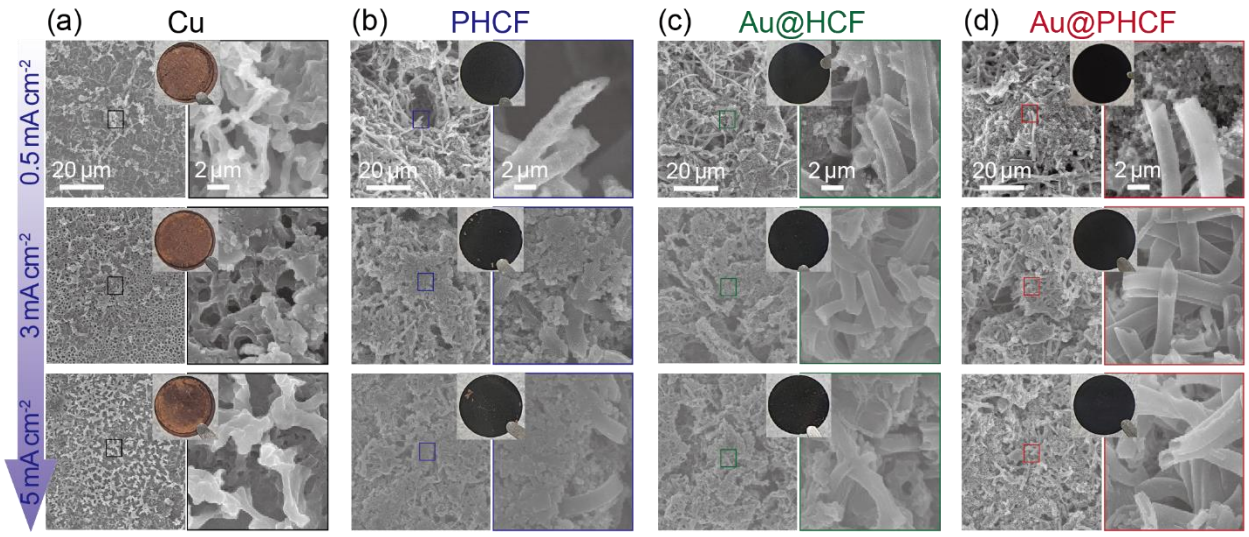

Figure S21. (a-d) SEM images of Cu, PHCF, Au@HCF, and Au@PHCF electrodes after the 1st Li stripping at different current densities of 0.5, 3, and 5 mA cm^{-2} with 1 mAh cm^{-2}. The right panel of (a-d) are magnified images from the colored boxes in the left panel. The insets in (a-d) are digital photographs of the test samples.

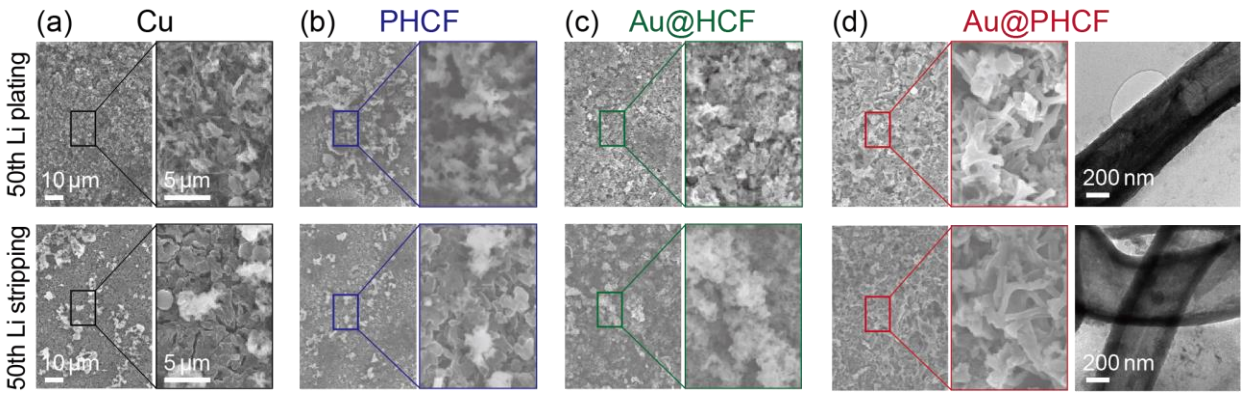

Figure S22. (a-d) SEM images of Cu, PHCF, Au@HCF, and Au@PHCF after the 50th Li plating/stripping at 5 mA cm^{-2} with 1 mAh cm^{-2}. The right panels of (d) are the TEM images of the Au@PHCF during the 50th cycle.

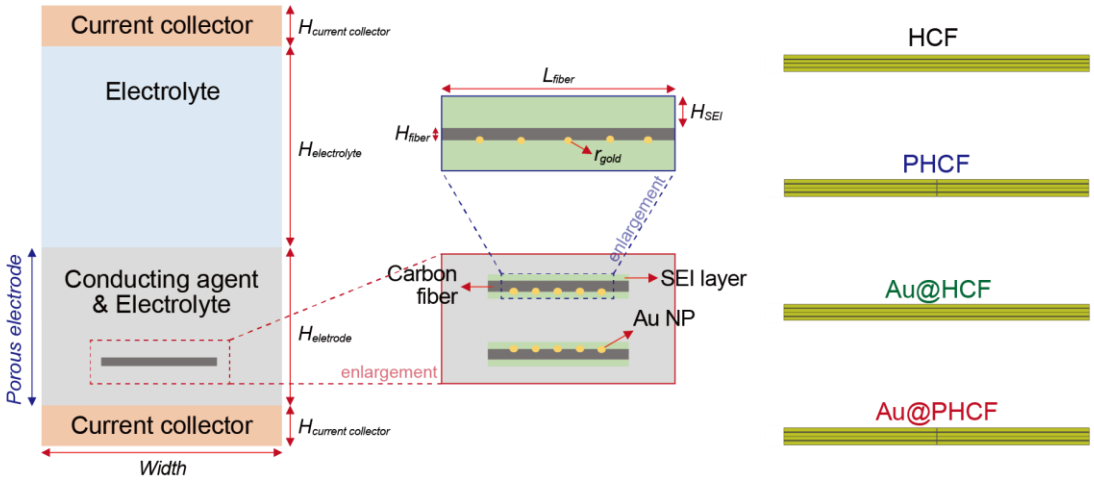

Figure S23. Schematic of Li asymmetric cell geometry with single carbon fiber. For the Au@HCF and Au@PHCF, the Au NPs were embedded inside hollow carbon fiber. For the PHCF and Au@PHCF, the shell pores were generated both side in 2D configuration. Ground connection was applied on one side current collector, and the current was applied on opposite side. It is assumed that the SEI layer is uniformly formed both inside and outside the fiber surface.

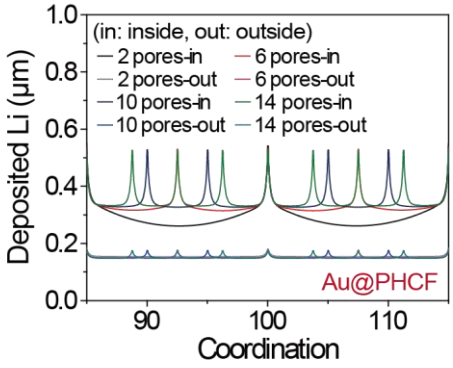

Figure S24. Deposited Li thickness inside and outside the Au@PHCF upon variation of generated pore number after Li plating at 0.1 mA cm^{-2} and 0.1 mAh cm^{-2}. In this simulation, a pair of pores face each other in the fiber.

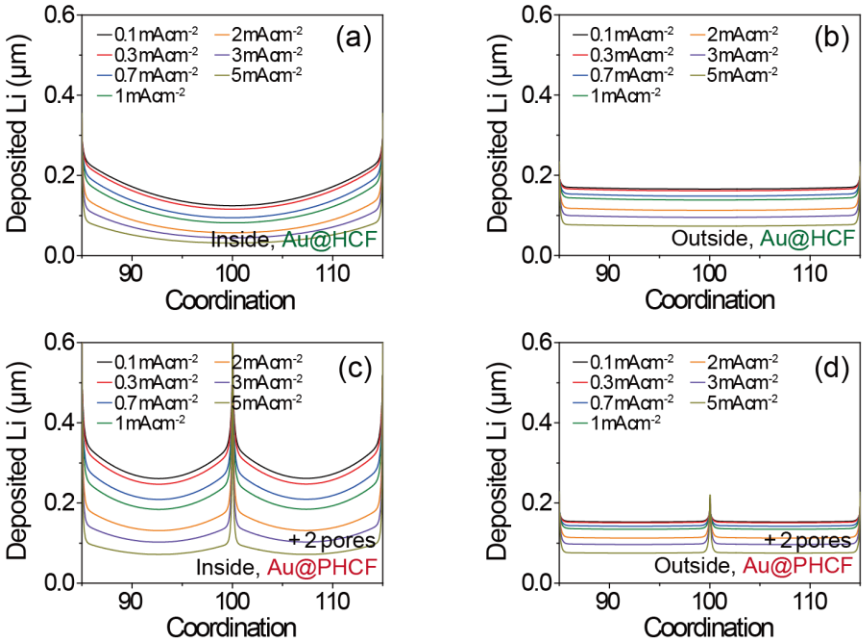

Figure S25. Deposited Li thickness (a, c) inside and (b, d) outside the Au@HCF and Au@PHCF, respectively, after Li plating with a capacity of 0.1 mAh cm^{-2}.

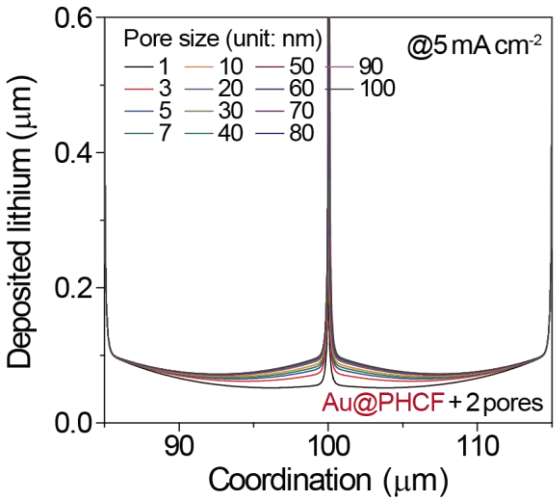

Figure S26. Distribution of deposited Li inside the Au@PHCF with various pore size from 1 to 100 nm at 5 mA cm^{-2}.

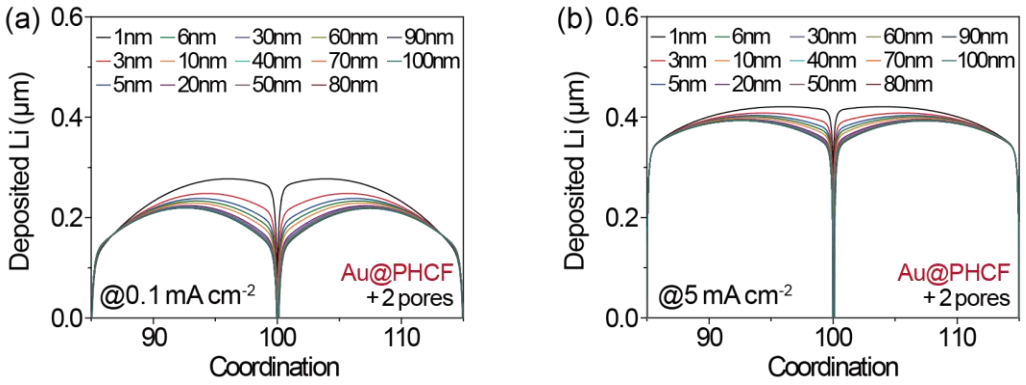

Figure S27. Remaining Li thickness inside the Au@PHCF with various pore size from 1 to 100 nm after Li stripping with a capacity of 0.1 mAh cm^{-2} at (a) 0.1 and (b) 5 mA cm^{-2}. Regardless of applied current densities, the Li stripping ability is saturated at near 10 nm in pore size. In this simulation, the initial deposited Li thickness was 0.48 μm.

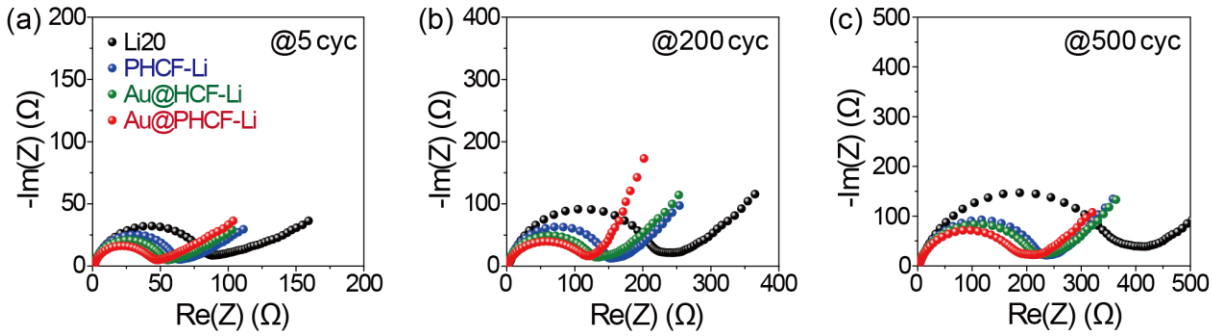

Figure S28. Nyquist plots for the LFP full cells shown in Figure 5a during 500 cycles.

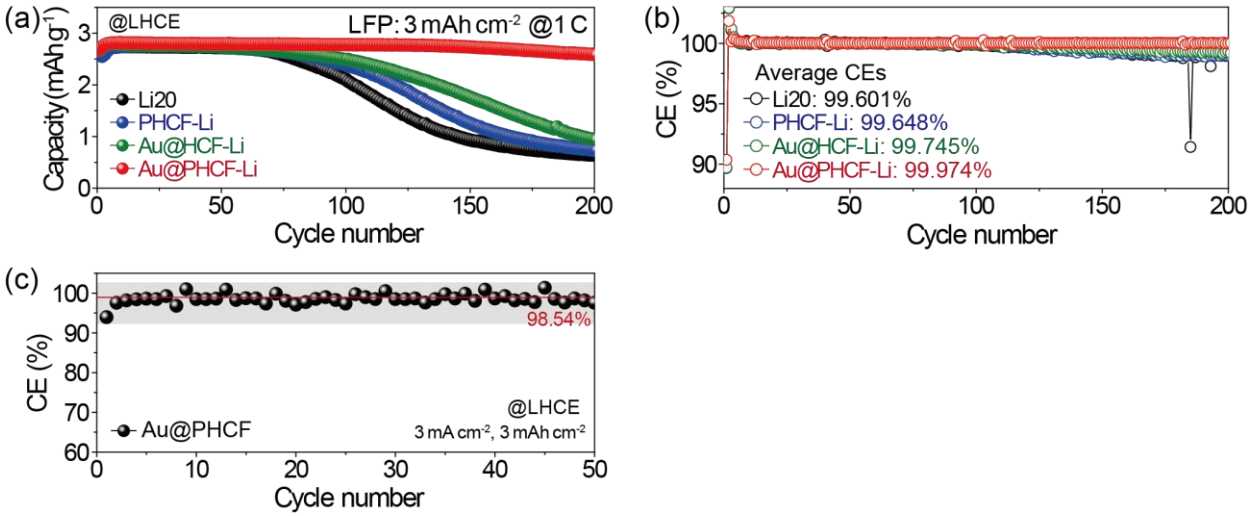

Figure S29. (a) Cycling performances and (b) corresponding CEs of 3 mAh cm^{-2} LFP full cells incorporating Li20, PHCF-Li, Au@HCF-Li, and Au@PHCF-Li anodes at 1 C. For the full cell tests, we predeposited 4 mAh cm^{-2} Li onto the PHCF, Au@HCF, and Au@PHCF to make Li-containing anodes. The average CEs in cycles 1 to 200 was indicated beside the legend texts. (c) CE of an asymmetric cell incorporating Au@PHCF electrode at 3 mA cm^{-2} with a constant capacity of 3 mAh cm^{-2}.

Note: In the diluent electrolyte, while the LFP/Au@PHCF-Li full cell showed a high CE of 99.974% and stable cycle life for 200 cycles (Figure S29a,b), the asymmetric Li/Au@PHCF cell exhibited a lower average CE of 98.54% at 3 mA cm^{-2} and 3 mAh cm^{-2} under test condition

similar to that of the full cell (Figure S29c). This discrepancy mainly originates from the different configurations of the two cells.[S3,S4] For the LFP/Au@PHCF-Li full cell, there was no significant capacity decay, and it showed a high CE because the anode with excess Li continuously supplied Li. According to previous reports,[S3,S4] for Li-metal full cell, when the active excess Li is exhausted, the capacity begins to decrease. Therefore, despite the average CE of 98.54% for the Li/Au@PHCF asymmetric cell, the LFP/Au@PHCF-Li cell exhibited a stable cycle life. In addition, the LFP full cells showed different cycle lives depending on the CEs of the anodes (Figures 2a-c and S29c), indicating a significant impact on the cycle life of the full cell due to the CE of the anode host. Additionally, if the deterioration at the cathode side is insignificant, and the amount of active Li loss in the Au@PHCF-Li anode of the full cell by dead Li formation and thickened SEI is calculated based on the average CE of the Au@PHCF host, a stable half cell-like operation with little capacity decay would theoretically be possible until 175 cycles.

Estimation of cycle life of the LFP full cell considering additional Li supply from Au@PHCF-Li: To focus on the active Li loss at the Au@PHCF-Li anode, we assumed that the deterioration at the cathode side is negligible. When 3 mAh cm^{-2} of Li from the cathode is first deposited on the prelithiated anode during charging, ~ 7 mAh cm^{-2} of Li is contained in the Au@PHCF-Li anode, which is a fully charged state in which the inside of the host is filled with metallic Li. Considering that 1.46% of the Li participating in the electrochemical reaction is consumed per cycle based on the average CE of 98.54% of the Au@PHCF host at 3 mA cm^{-2} and 3 mAh cm^{-2} (Figure S29c), a stable half cell-like operation is theoretically possible up to ~ 175 cycles until the active Li of Au@PHCF-Li is completely consumed, which is in line with the result in Figure S29a showing a gradual capacity decay after approximately 150 cycles, reflecting the irreversible reactions at the cathode and anode sides.

6.1544 mAh (capacity of Li predeposited on Au@PHCF, 4 mAh cm^{-2}, 14pi) + 3.97995 mAh (capacity of Li supplied from LFP cathode, 3 mAh cm^{-2}, 13pi) ≒ 3.97995 mAh (capacity participating in electrochemical reaction) × (1 - 0.9854) (Li loss rate at the anode per cycle) × 175 (cycle number)

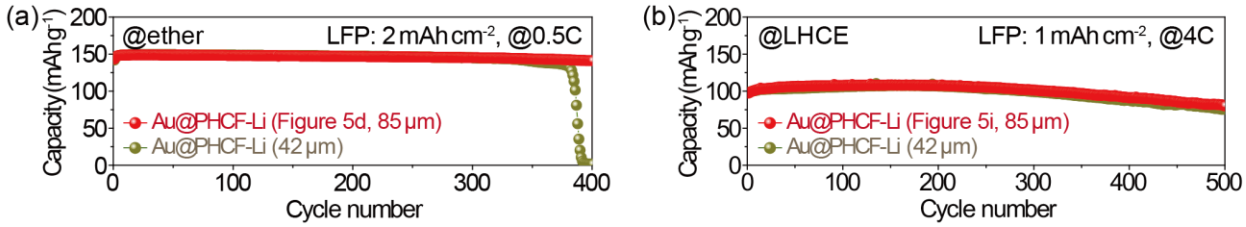

Figure S30. (a) Cycling performance of 2 mAh cm^{-2} LFP full cell with modified Au@PHCF-Li anode in an ether electrolyte at 0.5 C. (b) Cycling performance of 1 mAh cm^{-2} LFP full cell with modified Au@PHCF-Li anode in an LHCE electrolyte at 4 C. The results of the Au@PHCF-Li cells shown in Figure 5d and 5i (red color) are indicated for comparison. For this test, the Au@PHCF-Li electrode was prepared by plating 4 mAh cm^{-2} Li onto the Au@PHCF.

Note: For this test, to increase the volumetric energy density, an Au@PHCF-Li electrode with a reduced thickness of 42 μm (denoted as modified Au@PHCF-Li) was prepared through a roll-pressing process. In the case of Figure S30a, we tested a 2 mAh cm^{-2} LFP full cell considering the loading level of the Au@PHCF and residual empty space for Li storage of the Au@PHCF-Li. Despite the thickness reduction, the modified Au@PHCF-Li cells showed cycling trends similar to those of the Au@PHCF-Li cells shown in Figure 5d and 5i, which indicates that the anode thickness did not significantly affect the cell performance. In addition, owing to the reduced thickness, a higher volumetric energy density of 388.1 Wh L^{-1} (Figure S30a) was obtained compared to that of the original sample shown in Figure 5d (301.03 Wh L^{-1}, Table S1). For this calculation, we excluded the volume of the package foil.

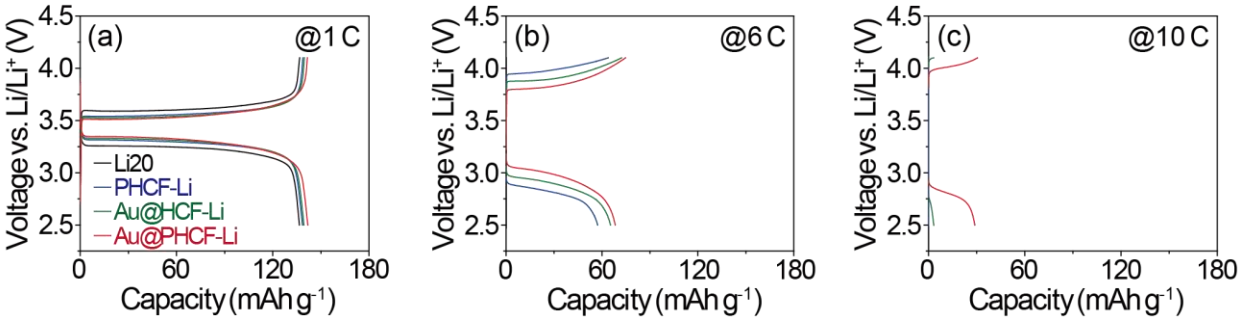

Figure S31. Voltage curves of the cells at (a) 1, (b) 6, and (c) 10 C during the rate performance tests shown in Figure 5g.

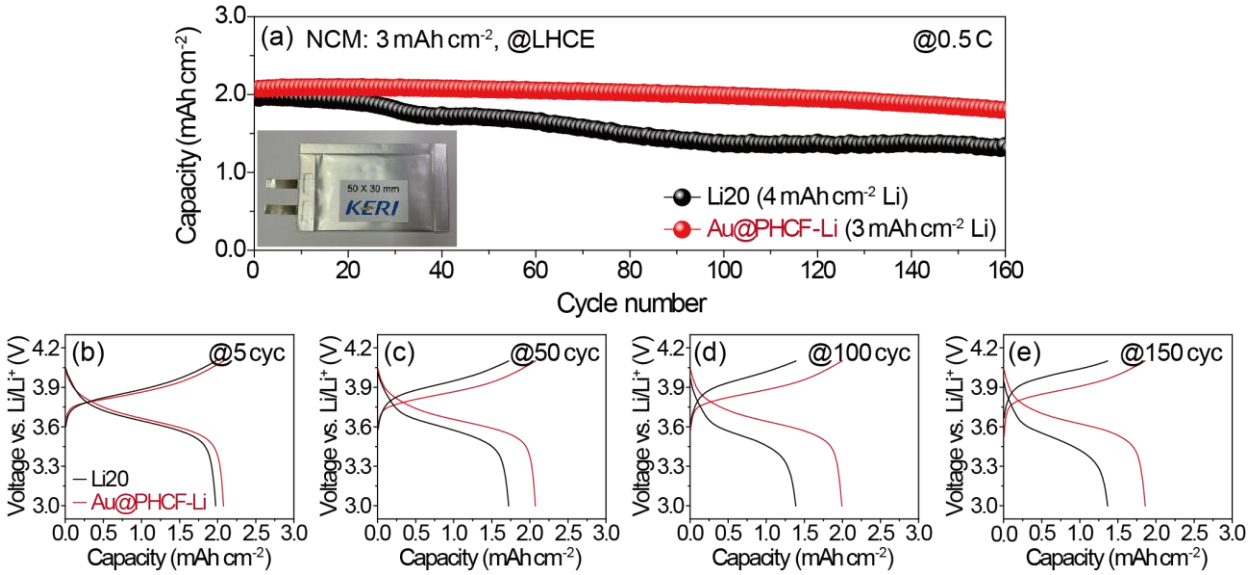

Figure S32. (a) Cycling performances and (b-e) voltage profiles of 3 mAh cm^{-2} NCM full cells with Li20 and Au@PHCF-Li anodes at 0.5 C. For this test, the Au@PHCF-Li was prepared by depositing 3 mAh cm^{-2} Li onto the Au@PHCF electrode, and the upper voltage cutoff was set to 4.1 V to avoid electrolyte decomposition.[S5]

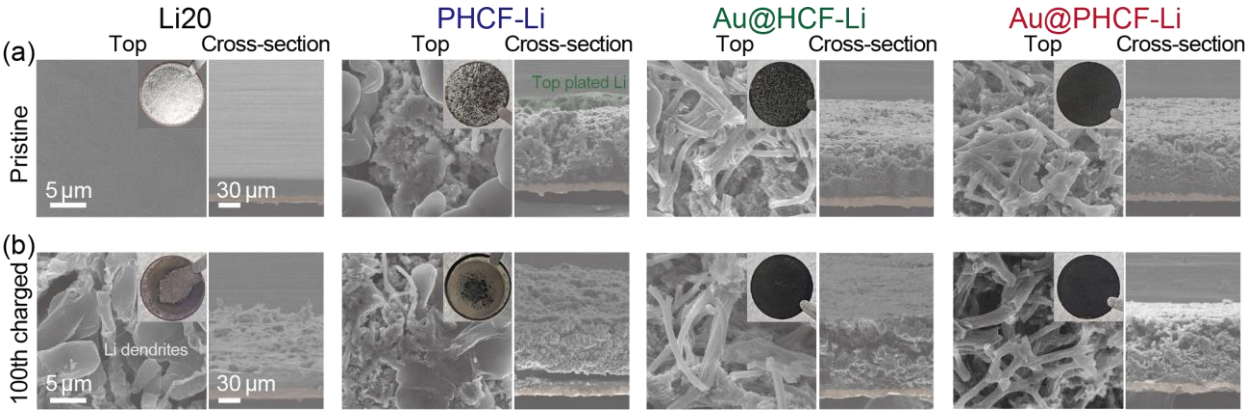

Figure S33. (Left panel) top-view and (right panel) cross-sectional SEM images of the anodes of LFP full cells shown in Figure 5a at the (a) pristine and (b) 100th charged states. The insets are digital photographs of the anodes.

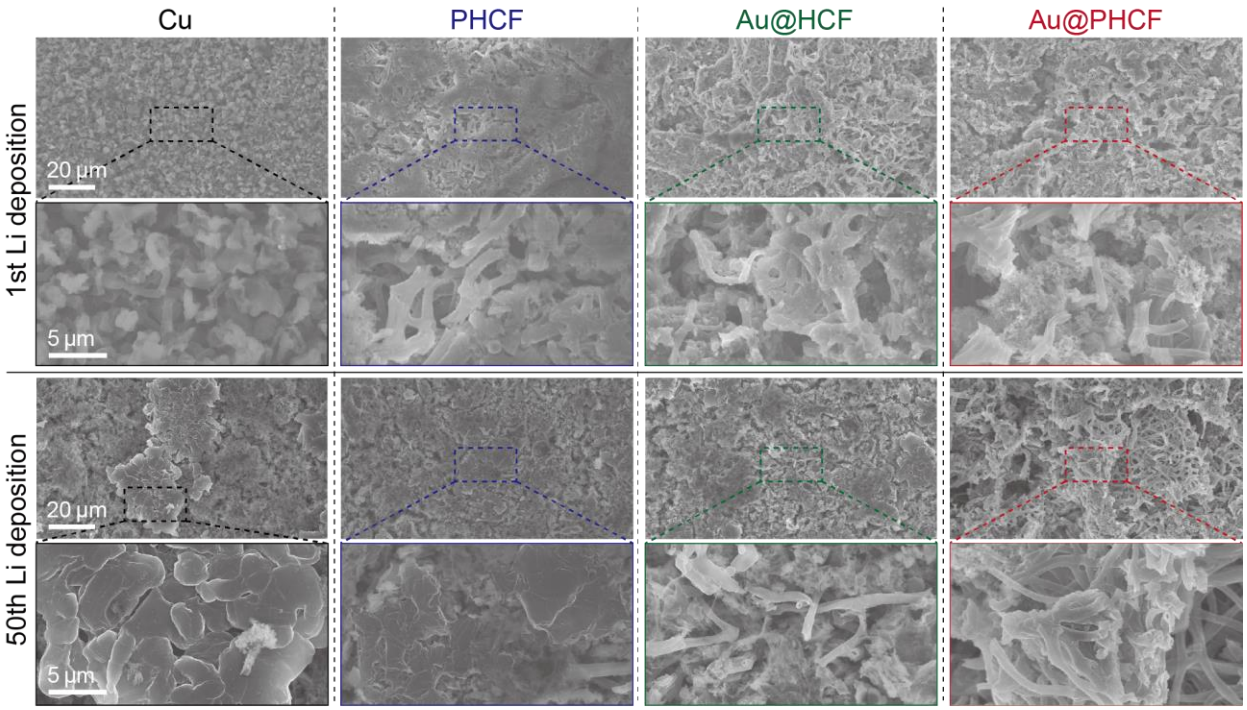

Figure S34. SEM images of electrodes of the asymmetric cells shown in Figure 2c after the 1st and 50th Li deposition in the LHCE electrolyte.

Table S1. Estimated energy densities of the single cells in this study.

		LFP / Au@PHCF-Li [Fig. 5a]	**LFP / Au@PHCF-Li [Fig. 5d]**	**LFP / Au@PHCF-Li [Fig. S29]**	**NCM811[a] / Au@PHCF-Li [Estimation]**	**NCM811[a] / Graphite [Estimation]**
Cathode areal capacity		1 mAh cm^{-2}	2 mAh cm^{-2}	3 mAh cm^{-2}	4.2 mAh cm^{-2}	4.2 mAh cm^{-2}
Discharge capacity		150 mAh g^{-1}	150 mAh g^{-1}	150 mAh g^{-1}	211 mAh g^{-1}	211 mAh g^{-1}
Average discharge voltage		3.353 V	3.353 V	3.353 V	3.84 V	3.64 V[d]
Weight	Al foil (15 μm, 13 mm dia.)	5.62 mg	5.62 mg	5.62 mg	5.62 mg	5.62 mg
	Cathode (Thickness, t)	11.037 mg (t = 38 μm)	22.073 mg (t = 76 μm)	33.11 mg (t = 114 μm)	28.45 mg (t = 64 μm)	28.45 mg (t = 64 μm)
	Separator (14 μm)	1.304 mg	1.304 mg	1.304 mg	1.304 mg	1.304 mg
	Electrolyte	170.45 mg	170.45 mg	170.45 mg	-	-
	Electrolyte (If E/C ratio[b] is 3 g Ah^{-1})	3.98 mg	7.96 mg	11.94 mg	16.72 mg	16.72 mg
	Anode (Thickness, t)	1.949 mg (t = 85 μm)	1.949 mg (t = 85 μm) (t = 42 μm)[c]	1.949 mg (t = 85 μm)	1.949 mg (t = 85 μm) (t = 42 μm)[c]	17.381 mg (n/p =1.1) (t: 45 μm)
	Cu foil (10 μm, 14 mm dia.)	13.67 mg	13.67 mg	13.67 mg	13.67 mg	13.67 mg
	Preloaded Li	1.594 mg (+4 mAh cm^{-2} Li)	1.594 mg (+4 mAh cm^{-2} Li)	1.594 mg (+4 mAh cm^{-2} Li)	1.196 mg (+3 mAh cm^{-2} Li)	-
	Al-pouch package foil[e]	93.2 mg	93.2mg	93.2mg	-	-
	Total cell weight	298.82 mg	309.86 mg	320.89 mg	-	-
	Total cell thickness without package foil	162 μm	200 μm (157 μm)[c]	238 μm	188 μm (145 μm)[c]	148 μm
	Total cell weight with 3 g Ah^{-1} electrolyte and without package foil	39.154 mg	54.17 mg	69.187 mg	68.909 mg	83.145 mg
Gravimetric energy density		14.86 Wh kg^{-1}	28.66 Wh kg^{-1}	41.52 Wh kg^{-1}	-	-
Gravimetric energy density with 3 g Ah^{-1} electrolyte and without package foil		113.42 Wh kg^{-1}	163.95 Wh kg^{-1}	192.55 Wh kg^{-1}	314.45 Wh kg^{-1}	247.03 Wh kg^{-1}
Volumetric energy density without package foil		181.55 Wh L^{-1}	301.03 Wh L^{-1} (388.1 Wh L^{-1})[c]	385.66 Wh L^{-1}	776.36 Wh L^{-1} (1018 Wh L^{-1})[c]	944.1 Wh L^{-1}

This table is based on the internal experimental results.

[a] Cell data of NCM811 (Reference S6).

[b] E/C ratio is defined as the ratio of the amount of electrolyte to the cathode capacity.

[c] The thickness of Au@PHCF after the roll-press process (Figure S30) and corresponding volumetric energy density.

[d] The average cell voltage of NCM811/graphite was assumed to be 0.2 V lower than that of the Li-metal cell based on a previous study (Reference S7).

[e] For calculation of total weight, the weight of the Al-pouch package foil was used instead of the coin-type cell case.

Calculation of theoretical and areal capacities of Au@PHCF: To obtain the volume information inside the Au@PHCF for storing metallic Li, we used a mercury porosimeter (AutoPore, Micromeritics, USA) and obtained a total volume of 3.5166 mL g^{-1}. Based on this value, the theoretical specific and areal capacities of Au@PHCF were calculated using the following simple equations:

[Eq. 1] Weight of Li that can be stored in Au@PHCF: 3.5166 cm^3 g^{-1} × 1.559 mg (weight of Au@PHCF on the Cu) × 0.53 g cm^{-3} (density of Li) = 2.906 mg

[Eq. 2] Total capacity of Li stored in Au@PHCF: 2.906 mg × 3860 mAh g^{-1} = 11.217 mAh

[Eq. 3] Theoretical specific capacity of full Li-containing Au@PHCF = 11.217 mAh / (1.559 + 2.906 mg) = 2512.2 mAh g^{-1}

[Eq. 4.] Theoretical areal capacity of full Li-containing Au@PHCF = 11.217 mAh / 1.5386 cm^2 (area of circular electrode) = 7.29 mAh cm^{-2}

The areal capacity can be varied depending on the loading level of Au@PHCF.

Note: As shown in Table S1, if we change the LFP to NCM cathode, increase the loading level of the active material as well as the number of stacks, and reduce the weight of the electrolyte, package foil, and current collector,[S6,S8,S9] the energy density of the current cell can be dramatically improved. In addition, as the Au@PHCF-Li anode exhibits higher specific and areal capacities than graphite anode under a similar loading level, relatively higher estimated gravimetric and volumetric energy densities can be obtained in the Au@PHCF cell compared to those of the Li-ion cell with a graphite anode. Moreover, because unwanted Li dendrite growth would be observed at a high Li plating rate of 5 mA cm^{-2},[S10] Au@PHCF is considered more competitive than graphite.

Table S2. Li asymmetric cell parameters used in simulation for this study.

Parameters	Symbols	Value	Reference
Electrolyte conductivity	σ_l	11 $[mS/cm]$	[S11]
Electrolyte salt diffusivity	D_l	1.1×10^{-9} $[m^2/s]$	[S11]
Transference number	t_+	0.55	[S12]
Activity dependence	$\frac{\partial lnf}{\partial lnc_l}$	1.5	[S12]
Electrolyte salt concentration	c_l	1,000 $[mol/m^3]$	
SEI layer conductivity	σ_{SEI}	$1.1 \times 10^{-6}[S/cm]$	[S2]
SEI layer salt diffusivity	D_{SEI}	$2.95 \times 10^{-10}[cm^2/s]$	[S2]
SEI transference number	$t_{+,SEI}$	0.363	[S2]
SEI activity dependence	$\frac{\partial lnf}{\partial lnc_l}$	0	[S2]
Current collector conductivity	σ_{cc}	$5.81 \times 10^7[S/m]$	[S2]
Carbon fiber conductivity	σ_{cf}	$2.5 \times 10^{-2}[S/cm]$	[S13]
Carbon additive conductivity	σ_{carbon}	$100[S/m]$	[S5]
Carbon additive volume fraction	ε_s	0.213	
Lithium density	ρ_{Li}	$534[kg/m^3]$	[S2]
Molar mass	M_{Li}	0.006941 $[kg/mol]$	[S2]
PHCF exchange current density	$i_{0,PHCF}$	0.0784 $[mA/cm^2]$	In this work
Au@HCF exchange current density	$i_{0,Au@HCF}$	0.1193[mA/cm^2]	In this work
Au@PHCF exchange current density	$i_{0,Au@PHCF}$	$0.2363[mA/cm^2]$	In this work
Current collector exchange current density	$i_{0,cc}$	0.15 $[mA/cm^2]$	[S14]

REFERENCES

S1. Botte, G. G.; Subramanian, V. R.; White, R. E., Mathematical modeling of secondary lithium batteries. *Electrochim. Acta* **2000,** *45*, 2595-2609.

S2. Vu, T. T.; Eom, G. H.; Lee, J.; Park, M.-S.; Moon, J., Electrolyte interface design for regulating Li dendrite growth in rechargeable Li-metal batteries: A theoretical study. *J. Power Sources* **2021,** *496*, 229791.

S3. Xiao, J.; Li, Q.; Bi, Y.; Cai, M.; Dunn, B.; Glossmann, T.; Liu, J.; Osaka, T.; Sugiura, R.; Wu, B.; Yang, J.; Zhang, J.-G.; Whittingham, M. S., Understanding and applying coulombic efficiency in lithium metal batteries. *Nat. Energy* **2020,** *5*, 561-568.

S4. Huang, C.-J.; Thirumalraj, B.; Tao, H.-C.; Shitaw, K. N.; Sutiono, H.; Hagos, T. T.; Beyene, T. T.; Kuo, L.-M.; Wang, C.-C.; Wu, S.-H.; Su, W.-N.; Hwang, B. J., Decoupling the origins of irreversible coulombic efficiency in anode-free lithium metal batteries. *Nat. Commun.* **2021,** *12*, 1452.

S5. Park, K. H.; Kang, D. W.; Park, J.-W.; Choi, J.-H.; Hong, S.-J.; Song, S. H.; Lee, S.-M.; Moon, J.; Kim, B. G., Modulating the electrical conductivity of a graphene oxide-coated 3D framework for guiding bottom-up lithium growth. *J. Mater. Chem. A* **2021,** *9*, 1822-1834.

S6. Niu, C.; Pan, H.; Xu, W.; Xiao, J.; Zhang, J.-G.; Luo, L.; Wang, C.; Mei, D.; Meng, J.; Wang, X.; Liu, Z.; Mai, L.; Liu, J., Self-smoothing anode for achieving high-energy lithium metal batteries under realistic conditions. *Nat. Nanotechnol.* **2019,** *14*, 594-601.

S7. Martin, C.; Genovese, M.; Louli, A. J.; Weber, R.; Dahn, J. R., Cycling Lithium Metal on Graphite to Form Hybrid Lithium-Ion/Lithium Metal Cells. *Joule* **2020,** *4*, 1296-1310.

S8. Heubner, C.; Maletti, S.; Auer, H.; Hüttl, J.; Voigt, K.; Lohrberg, O.; Nikolowski, K.; Partsch, M.; Michaelis, A., From Lithium-Metal toward Anode-Free Solid-State Batteries: Current Developments, Issues, and Challenges. *Adv. Funct. Mater.* **2021,** *31*, 2106608.

S9. Chen, S.; Niu, C.; Lee, H.; Li, Q.; Yu, L.; Xu, W.; Zhang, J.-G.; Dufek, E. J.; Whittingham, M. S.; Meng, S.; Xiao, J.; Liu, J., Critical Parameters for Evaluating Coin Cells and Pouch Cells of Rechargeable Li-Metal Batteries. *Joule* **2019,** *3*, 1094-1105.

S10. Lee, S.-M.; Kim, J.; Moon, J.; Jung, K.-N.; Kim, J. H.; Park, G.-J.; Choi, J.-H.; Rhee, D. Y.; Kim, J.-S.; Lee, J.-W.; Park, M.-S., A cooperative biphasic MoO_x–MoP_x promoter enables a fast-charging lithium-ion battery. *Nat. Commun.* **2021,** *12*, 39.

S11. Park, C.; Kanduč, M.; Chudoba, R.; Ronneburg, A.; Risse, S.; Ballauff, M.; Dzubiella, J., Molecular simulations of electrolyte structure and dynamics in lithium–sulfur battery solvents. *J. Power Sources* **2018,** *373*, 70-78.

S12. Safari, M.; Kwok, C. Y.; Nazar, L. F., Transport Properties of Polysulfide Species in Lithium–Sulfur Battery Electrolytes: Coupling of Experiment and Theory. *ACS Cent. Sci.* **2016,** *2*, 560-568.

S13. Qin, W.; Vautard, F.; Drzal, L. T.; Yu, J., Mechanical and electrical properties of carbon fiber composites with incorporation of graphene nanoplatelets at the fiber–matrix interphase. *Compos. B. Eng.* **2015,** *69*, 335-341.

S14. Guo, F.; Wu, C.; Chen, S.; Ai, X.; Zhong, F.; Yang, H.; Qian, J., Flaky and Dense Lithium Deposition Enabled by a Nanoporous Copper Surface Layer on Lithium Metal Anode. *ACS Mater. Lett.* **2020,** *2*, 358-366.